Statistical significance of small ensembles of simulations and detection of the internal climate variability: An excitable ocean system case study

Stefano Pierini[1,2]

1 Dipartimento di Scienze e Tecnologie, Università di Napoli Parthenope, Naples, Italy

2 CoNISMa, Rome, Italy

Pierini S., 2020: Statistical significance of small ensembles of simulations and detection of the internal climate variability: An excitable ocean system case study.

Journal of Statistical Physics, **179**, 1475-1495.

Published in the Special Issue on the *Statistical Mechanics of Climate*

https://doi.org/10.1007/s10955-019-02409-x.

Received: 27 August 2019 / Accepted: 16 October 2019

Corresponding author address: Stefano Pierini, Dipartimento di Scienze e Tecnologie, Università di Napoli Parthenope, Centro Direzionale, Isola C4, 80143 Napoli, Italy

(stefano.pierini@uniparthenope.it)

Abstract

The correct mathematical approach to climate change requires the knowledge of the time-dependent system's pullback/snapshot attractor (PBA). Once the governing equations and external forcing are known, the PBA can be estimated by performing an ensemble simulation (ES) of many forward time integrations differing only by their respective initialization; the resulting ensemble mean and spread are usually considered as representative of the forced and internal variability (FV and IV), respectively. In this paper the PBA of an excitable conceptual ocean model subjected to an idealized decadal time-scale aperiodic forcing is determined and is then used to show that the system's relaxation oscillations contribute substantially to the ensemble mean, despite their intrinsic nature: as a consequence, a clear separation between the FV and IV is impossible in this case study. This provides an example of dynamical behaviour which may be typical of climate ESs under fluctuating aperiodic forcing. The impact of the number of ensemble members N on the statistical significance of the ES is then investigated. The complexity of realistic climate modelling currently imposes N=O(100): how significant is the statistical information derived from such small ESs? To answer this question for the present case study, the knowledge of the PBA is exploited to carry out a systematic comparison between the latter and small ESs with N=50, also by using novel quantifiers specifically conceived for this purpose. The results reveal a remarkable significance of such ESs beyond the predictability time and may provide useful information for the design of future realistic ESs.

Keywords:

Pullback attractors · Ensemble simulations · Climate change · Internal climate variability · Reduced order climate models · Excitable systems

1 Introduction

It has recently been recognized that the correct description of a changing climate subjected to both natural and anthropogenic forcing requires the knowledge of the time-dependent probability distributions associated with the system's *pullback* (or, alternatively, but equivalently, *snapshot*) *attractor* (PBA) [1-16]. The resulting description can be considerably different [13] from the classical one based on the 30-yr temporal average of a single long time series of climatological data [17], whether observed or simulated numerically: this is basically due to the nonergodicity of aperiodically forced systems [18].

The PBA is a mathematical tool which provides the extension to a nonautonomous system of the classical concept of attractor of a nonlinear dissipative autonomous dynamical system [e.g., 19-23]. If the external forcing and/or some parameter depend on time, the PBA is the subset $A(t)$ of phase space which, together with the probability measure supported on this set, is invariant under the governing equations and is such that any trajectory initialized in the remote past converges to it [e.g., 1,10].

In a numerical approach, the PBA and corresponding time-dependent probability measure can be estimated by performing an ensemble of many forward time integrations differing only by their respective initialization. The ensemble simulations (ESs) appropriate for the description of long-term climate changes and suitable for estimating the PBA require, therefore, climate model integrations longer than the predictability time, so that the memory of the initialization is lost thanks to the system's chaoticity. In contrast, the more classical ESs preformed for weather forecasting are typically shorter or comparable than the predictability time, so that some memory of the initialization is retained. ESs for weather forecasting and climate change studies differ also in that, while for the former the ensemble spread is a measure of the uncertainty of the simulation, in the latter it is linked with the system's internal (or intrinsic) variability (IV) and is, therefore, an irreducible property of the climate system. In this case, the ensemble members can be seen as independent *parallel climate*

realizations [15] subjected to the same governing equations, boundary conditions and forcing but each emerging from a different initial condition and characterized by a given probability of occurrence.

The analysis of the PBAs of the climate system and of its subsystems is a recent field of research; thus, several theoretical and applicative aspects are still currently under debate and need to be clarified. In this context, the present paper focuses on two fairly general and interrelated issues, that will be investigated in the framework of the wind-driven ocean circulation [24,25], through an idealized case study based on a four-variable excitable model [26] subjected to an aperiodic external forcing having both a decadal time-scale variability as well as higher frequency fluctuations.

The first issue (i) concerns the identification of the system's IV. In long-term climate change simulations the nonautonomous nature of the system is typically associated with temporal drifts imposed on some parameters, such as the CO_2 concentration [e.g., 10,13,15]: in such a situation the IV and forced variability (FV) are well represented by the ensemble spread and mean, respectively. In other recent PBA numerical model studies [14,27], ES *hindcasts* are instead performed in which the excitable [28-30] conceptual ocean model [26] is forced by an idealized aperiodic surface wind field possessing decadal time scales that are comparable to those of the system's intrinsic relaxation oscillations (ROs [31,30]). In this case the forcing can pace or even excite the ROs, which can therefore contribute substantially to the FV despite their intrinsic nature; as a consequence, a clear separation between the IV and FV is not possible in this case. This subtle and general issue, relevant in particular for climate ESs under fluctuating forcing, will be investigated in our idealized case study by making direct reference to the system's PBA.

The second issue (ii) concerns the impact of the number of ensemble members N on the statistical significance of the ES. In the analysis of conceptual models with few degrees of freedom, thanks to the limited computational cost of the numerical integrations an $N = O(10^4 \div 10^9)$ can be adopted [e.g., 3,14,27,10], in which case the PBA and its natural probability measure can be estimated accurately. On the other hand, for more realistic climate systems, only single-model ESs with a

limited number of members [$N = O(10^2)$] can currently be carried out; for example, $N = 40$ in [13], $N = 192$ in [15], $N = 50$ in [32], $N = 100$ in [33]. In these cases a question arises: to what extent is the resulting statistical information representative of the PBA, whose detailed structure remains unknown? To this respect, it could be useful to develop a process study in which small ESs are systematically compared with the PBA in a case in which the latter can be determined, that is, if the system is governed by a conceptual model. Although the obtained results could not be directly extended to realistic models, they could nonetheless provide useful information for designing future realistic model ESs. An analysis of this kind is carried out here (for the first time, at the best of the author's knowledge) in the framework of our idealized case study.

The paper is organized as follows. In section 2 the mathematical model, its autonomous behaviour and the adopted ensemble simulation strategy are presented. In section 3 the system's PBA is derived and the IV and FV are investigated [issue (i)]. Three small ESs are presented in section 4 and two additional small ESs are presented in section 5 to analyse sensitivity to initial data; in both sections comparison with the PBA is carried out [issue (ii)]. Still in the framework of issue (ii), in section 6 an analysis of the convergence of the small ESs to the PBA, also based on novel quantifiers specifically conceived for this purpose, is presented. Finally, in section 7 conclusions are drawn.

2 The mathematical model and the ensemble simulation strategy

2.1 The model

The conceptual ocean model [26] used in this study was derived to complement, with an agile mathematical tool, a series of model studies of the Kuroshio Extension (KE) low-frequency variability (LFV) performed with a reduced-gravity primitive equation ocean model [e.g., 34-36]. Thanks to its efficient computational cost, the same low-order model was later used for several theoretical studies that could not have been carried out with primitive equation models [37,38]. In addition, the same model was adopted to represent the ocean dynamics in low-order climate models

[39,40]. For all the technical details the reader should refer to [26]; here only the main mathematical aspects are recalled.

The system is governed by the evolution equation of potential vorticity in the quasigeostrophic approximation on the beta-plane and in the reduced-gravity approximation [e.g., 41] for a fluid contained in a rectangular domain with dimensionless coordinates $x, y \in [0, \pi]$. After a severe truncation of a Galerkin projection of these partial differential equations one gets the following system of four coupled nonlinear ordinary differential equations for the variables $[\Psi_1(t), \Psi_2(t), \Psi_3(t), \Psi_4(t)]$ [26]:

$$\frac{d\mathbf{\Psi}}{dt} + \mathbf{\Psi J \Psi} + \mathbf{L\Psi} = G(t)\mathbf{w}. \quad (1)$$

For the definition of the various coefficients summarized by the rank-3 tensor **J** and rank-2 tensor **L**, for the vector **w** representing the double-gyre surface wind stress curl forcing (assumed, in the present idealized framework, to be the same for both the mean and variable components) and for all the parameter values the reader should, again, kindly refer to [26].

In the present study, the time dependence $G(t)$ of the atmospheric forcing in (1) is defined as follows:

$$G(t) = \gamma\left\{1 + H_{LF}(t) + H_{HF}(t) + \varepsilon_3 \frac{\zeta_3(t)}{\sigma_3}\right\}; \quad H_{LF}(t) = \varepsilon_1 F_{T_f}\left[\frac{\bar{\zeta}_1(t)}{\sigma_1}\right]; \quad H_{HF}(t) = \varepsilon_2 \frac{\bar{\zeta}_2(t)}{\sigma_2} \quad (2)$$

where $\gamma = 1.1, \varepsilon_1 = 0.2, \varepsilon_2 = 0.1$, ε_3 is a positive dimensionless constant, $\bar{\zeta}_1$, $\bar{\zeta}_2$ (used throughout the present study) and ζ_3 are specific realizations (with σ_1, σ_2 and σ_3 their respective standard deviations) of red noise processes with decorrelation times $T_{s1} = 15\ years, T_{s2} = 1\ year$ and T_{s3}, respectively. In H_{LF}, F_{T_f} is a sliding window filter of width $T_f = 15\ years$ and the realization $\bar{\zeta}_1$ is the same adopted by [14], so that $\gamma(1 + H_{LF})\mathbf{w}$ is the same forcing used in one of their two reference simulations (see section 2b and Figs. 2a and 2c,e therein). Finally, for the sake of simplicity, in the discussion the following positions will be used:

$$H(t) = 1 + H_{LF}(t) + H_{HF}(t); \quad h(t) = \varepsilon_3 \frac{\zeta_3(t)}{\sigma_3}, \tag{3}$$

so that $G = \gamma(H + h)$. In summary, $\gamma\mathbf{w}$ is associated with the climatological time-independent forcing, $\gamma H_{LF}\mathbf{w}$ is the smooth low-frequency forcing of [14] (representing a schematic North Pacific multidecadal variability), $\gamma H_{HF}\mathbf{w}$ adds a high-frequency component to the forcing and the random perturbation $\gamma h\mathbf{w}$, used as an auxiliary noise for technical purpose, will be discussed in section 4.3. Finally, all the noises satisfy the Ornstein-Uhlenbeck stochastic differential equation characterized by a decorrelation time T_s. In Fig. 1 the thick line shows $(1 + H_{LF})$ (corresponding to Fig. 2a of [14]) while the thin line gives the total time dependence $G/\gamma = H$ for a specific realization $\overline{\zeta_2}(t)$ in H_{HF}, which will be used throughout the present study. It is worth noting that, while all the dependent variables and (x, y) are dimensionless, the time t is kept dimensional (as in Fig. 1 and in all the remaining figures) to stress the typical time scales of the oceanographic phenomenon (the KE LFV) that has inspired the low-order model, which are correctly reproduced by the latter.

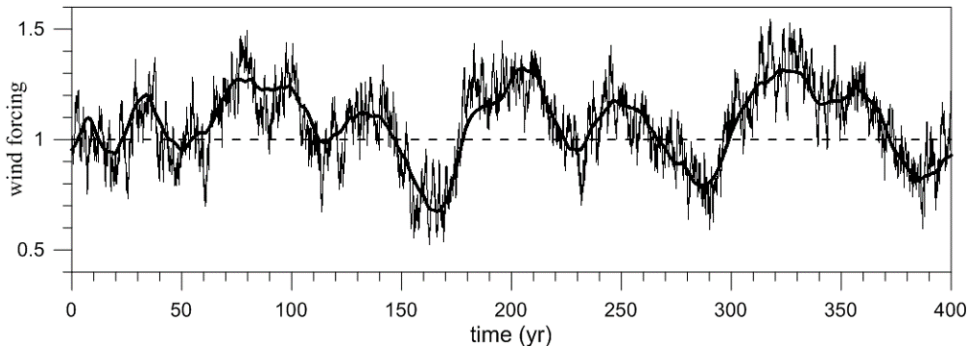

Fig. 1 Thick line: $(1 + H_{LF})$ defined in (2,3) representing a schematic North Pacific multidecadal variability. Thin line: total time dependence $G/\gamma = H$.

2.2 The autonomous system's behaviour

Here the behaviour of the autonomous version of model (1) (i.e., with $\varepsilon_1 = \varepsilon_2 = \varepsilon_3 = 0$ in (2)) is considered in the framework of dynamical systems theory. The bifurcation diagram of Fig. 2a is obtained by performing many forward time integrations, all initialized from rest, and shows the range of variability of Ψ_1 vs. the forcing amplitude γ. The first Hopf bifurcation, marking the transition

from a steady state to a limit cycle, occurs at $\gamma = 0.348$, but it is only for $\gamma \gtrsim 0.94$ that the limit cycle becomes of appreciable amplitude; the critical value $\gamma = 1$ marks the tipping-point transition from small amplitude oscillations to large amplitude ROs. Fig. 2b shows the map of the decimal logarithm of the probability p of localization of the trajectories in the (Ψ_1, Ψ_3) plane (see section 3 for an exact definition of this quantity) in the case $\gamma = 1.1$, while in Fig. 2c a sequence of snapshots of the streamfunction ψ for $\gamma = 1.043$ illustrates the spatial character of a typical RO; as discussed in [26], this oscillation provides a conceptual minimal model of the KE LFV.

To study the transition of the autonomous model (1) from limit cycles to strange attractors, a new diagnostic method based on ESs performed with the same model and forcing but with different initial data, has been recently proposed [27]. The system is found to be periodic, except for limited intervals centred at $\gamma \cong 1.25$ and $\gamma \cong 1.335$, until an abrupt transition to chaos occurs at $\gamma = 1.3475$.

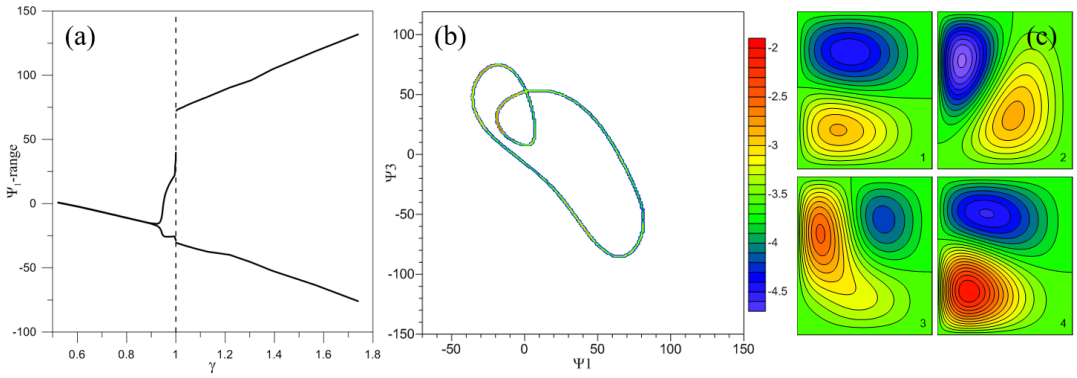

Fig. 2 (a) Bifurcation diagram of the autonomous ocean model; the range of variability of Ψ_1 after spinup is plotted vs. γ (adapted from [26]. (b) Map of the decimal logarithm of the probability of localization of the trajectories in the (Ψ_1, Ψ_3) plane for γ=1.1 (white colour corresponds to minus infinity, i.e., to boxes in which no trajectory happened to fall). (c) Sequence of snapshots of ψ for γ=1.043 with time increment of 4 $years$ illustrating the spatial structure of a typical RO (adapted from [38]).

2.3 The ensemble simulation strategy

A large ES and several small ESs are performed: the former is used to obtain the PBA and to investigate issue (i) while the latter are used to investigate issue (ii). Since, as already discussed in sections 2.1 and 2.2, the governing equations (1) are the same used in [14,27], the same number of ensemble members $N = 15{,}000$ and the same distribution of the initial data at $t_0 = 0$ (small black

dots in Fig. 3a) will be used to estimate the PBA with the ES ES0 (Table 1): this has the advantage to allow for an easier comparison with the previous results.

As for the small ESs (ES1-6), in consideration of the oceanographic nature of model (1), the same number of members used in the global oceanographic NEMO hindcasts [32] ($N = 50$) is adopted. The initial data will be produced following a classical approach, as follows. First, it is assumed (for ES1 and ES4) that the system lies at a given arbitrary point P_0 (belonging to the PBA) at $t_0 = 200\,years$. Then, 50 integrations, all starting from P_0, are carried out for $20\,years$, each being perturbed by an h, defined in (3), with a different noise realization. The 50 final states thus obtained will constitute the initial data for ES2-3 (black dots in Fig. 7b) and ES5-6 (black dots in Fig. 13b), as summarized in Table 1.

Ensemble simulation	**Number of ensemble members**	**G/γ**	ε_3	T_{s3} $(years)$	t_0; t_1 $(years)$	**Initial data from:**	$Z = \frac{\sigma_{MEV}}{\sigma_{ESV}}$
ES0	15,000	H	-	-	0; 400	Γ	0.73
ES1	50	$H + h$	0.2	0.5	200; 220	P_0 (ES0)	-
ES2	50	H	-	-	220; 280	ES1	0.60
ES3	50	$H + h$	0.1	1.0	220; 280	ES1	0.32
ES4	50	$H + h$	0.05	0.5	200; 220	P_0 (ES0)	-
ES5	50	H	-	-	220; 280	ES4	0.99
ES6	50	$H + h$	0.1	1.0	220; 280	ES4	0.41

Table 1 List of the ensemble simulations carried out in the present study. For the definition of H and h see section 2.1; the parameters ε_3 and T_{s3} refer to the auxiliary noise h.

3 The system's pullback attractor

If the external forcing and/or some parameter depend on time, a time-dependent subset $A(t)$ of phase space exists which is, together with the probability measure supported on this set, invariant under the governing equations and to which any trajectory, initialized in the remote past, converges: in this case

$A(t)$ is called the system's PBA (e.g., see [42,43] for rigorous mathematical treatments and [1,3] for a more accessible mathematical introduction in the framework of climate dynamics).

Thus, the PBA $A(t)$ provides the natural extension, to a nonautonomous system, of the attractors of autonomous systems, and is the set of all possible states the system -governed by a specific set of equations and driven by a specific external time-dependent forcing- can assume at time t.

How can a PBA be determined? Its very definition suggests how to proceed in a numerically based approach: the ensemble of trajectories obtained by forward time integration of many different initial states starting from $t = t_0$ provides a good approximation of $A(t)$ for a sufficiently remote t_0. This approach was recently followed in [38,14,27] to study several properties of system (1) that are likely to be generic of nonautonomous dynamical systems; other recent studies are carried out in the same context [e.g., 4,44,10].

A limited number (750) of trajectories initialized at $t_0 = 0$ and integrated for $t_{lim} = 400\ years$ provides, in Fig. 3a, a graphical representation of the PBA of system (1) subjected to the forcing $\gamma H\mathbf{w}$ [see the thin line of Fig. 1 for $H(t)$]. On the other hand, to obtain a significant estimate of the PBA, in the ES denoted ES0 (Table 1) many more trajectories ($N = 15{,}000$) are initialized at $t_0 = 0$ in a subset Ω of phase space defined as follows:

$$\Psi_1, \Psi_2 \in [-70{,}150];\ \ \Psi_3, \Psi_4 \in [-150{,}120]. \qquad (4)$$

Following [26], the conditions $\Psi_1 = \Psi_2$ and $\Psi_3 = \Psi_4$ are imposed at t_0. For the sake of graphical clarity, only $\Psi_1(t)$ and $\Psi_3(t)$ contained in the rectangle $\Gamma = \{-70 \leq \Psi_1 \leq 150, -150 \leq \Psi_3 \leq 120\} \subset \Omega$ are shown throughout the paper. [14] showed that the same system subjected to the LF forcing given by the thick line of Fig. 1 yields a transient of about $15 \div 20\ years$; analogously, here the trajectories can be considered to be representative of the PBA for $t \gtrsim 20\ years$.

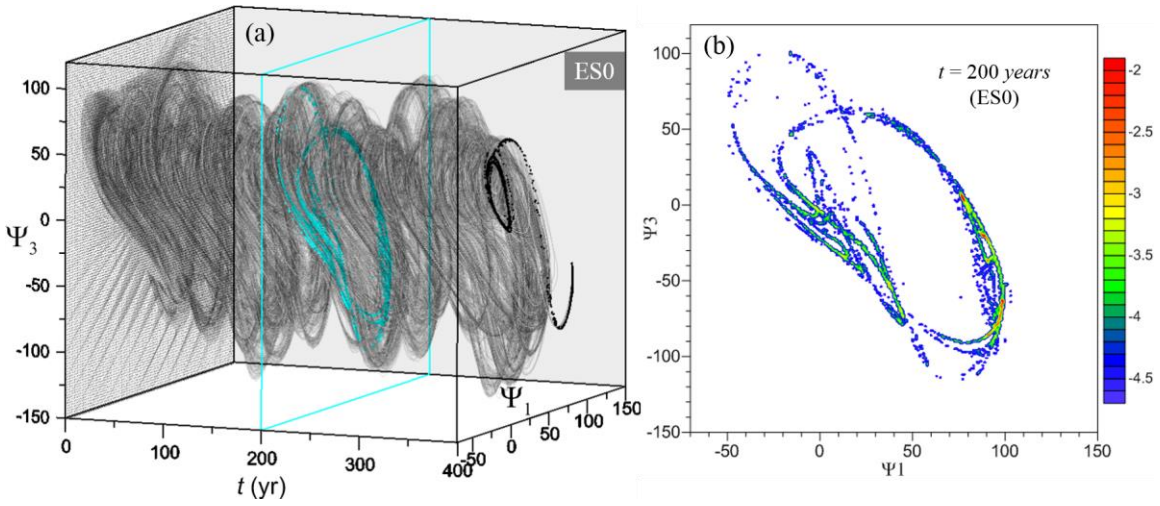

Fig. 3. (a) Grey lines: graphical representation (750 trajectories) of the PBA of system (1) subjected to the forcing $\gamma H\mathbf{w}$; in the same panel the intersection of the PBA –as determined by 15,000 trajectories– with Γ is shown at t =0 (black dots), $t = 200\,years$ (cyan dots) and $t = 400\,years$ (black dots). (b) Map of the decimal logarithm of the probability of localization of the PBA trajectories, P_i in Γ at $t = 200\,years$ (white colour corresponds to minus infinity).

In the same Fig. 3a, the intersection of the PBA with Γ is shown at $t = 0, 200, 400\,years$ by black, cyan and, again, black dots, respectively. Finally, Fig. 3b shows the map of $P_i(t) = \log_{10} p_i(t)$ at $t = 200\,years$, where $p_i = n_i/N$ is the probability of localization of the trajectories within Γ (n_i is the number of trajectories contained -at time t- in the i-th cell belonging to the square grid with steps $\Delta\Psi_1 = \Delta\Psi_3 = 1$). Moreover, following [14,27], a statistical characterization of the PBA is provided, for Ψ_3, by the map of Fig. 4a, showing the decimal logarithm of the probability of localization of the trajectories $P_{\Psi_3}(t)$ as a function of time for ES0 (the adopted normalization is described in [14]).

In Fig. 4b the thick line denotes the ensemble mean $\langle\Psi_3\rangle(t)$ computed over the members $\Psi_3^{(k)}(t)$, $k = 1, \ldots, N$ (from now on, $\langle\cdot\rangle \equiv \sum_k^N \cdot /N$), while the grey shading shows the interval $2\sigma_{\Psi_3}$ centred around $\langle\Psi_3\rangle$, where σ_{Ψ_3} is the ensemble standard deviation:

$$\sigma_{\Psi_3}(t) = \sqrt{\langle[\Psi_3(t) - \langle\Psi_3\rangle(t)]^2\rangle}\,. \tag{5}$$

Besides, the mean ensemble variability (MEV) and ensemble spread variability (ESV) are introduced:

$$\sigma_{MEV} = \sqrt{\overline{\left[\langle\Psi_3\rangle(t) - \overline{\langle\Psi_3\rangle}\right]^2}};\quad \sigma_{ESV} = \sqrt{\overline{\langle[\Psi_3(t) - \langle\Psi_3\rangle(t)]^2\rangle}};\quad Z = \frac{\sigma_{MEV}}{\sigma_{ESV}} \tag{6}$$

where the overbar indicates temporal mean over the 400 years-long time series. The result for ES0 is:

$\sigma_{MEV} = 29.0;\ \sigma_{ESV} = 39.8;\ Z = 0.73.$

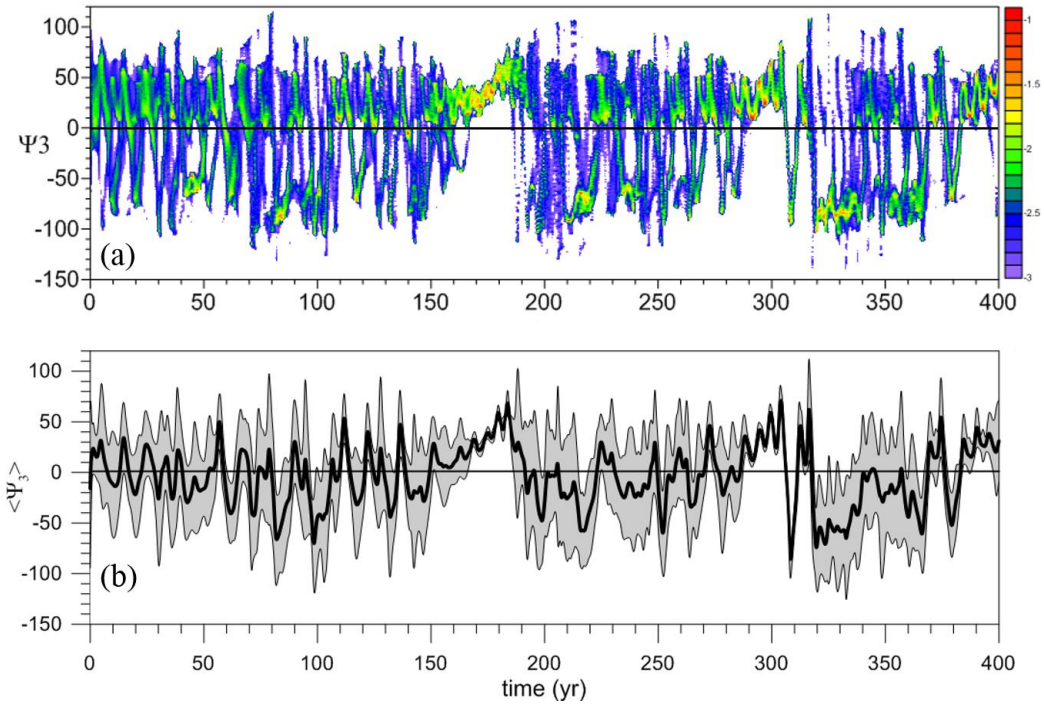

Fig. 4 (a) Probability of localization of the trajectories $P_{\Psi_3}(t)$ for ES0 (white colour corresponds to minus infinity). (b) Thick line: ensemble mean $\langle\Psi_3\rangle$. Grey shading: interval of twice the ensemble standard deviation σ_{Ψ_3} centred around $\langle\Psi_3\rangle$.

It is customary to use σ_{MEV} (σ_{ESV}) as a measure of the FV (IV), e.g., as done in [45] with reference to the NEMO-ES [32]. However, these two forms of variability cannot be unambiguously separated due to the nonlinear nature of the system. Fig. 5 is used to clarify this issue [(i), see the Introduction]

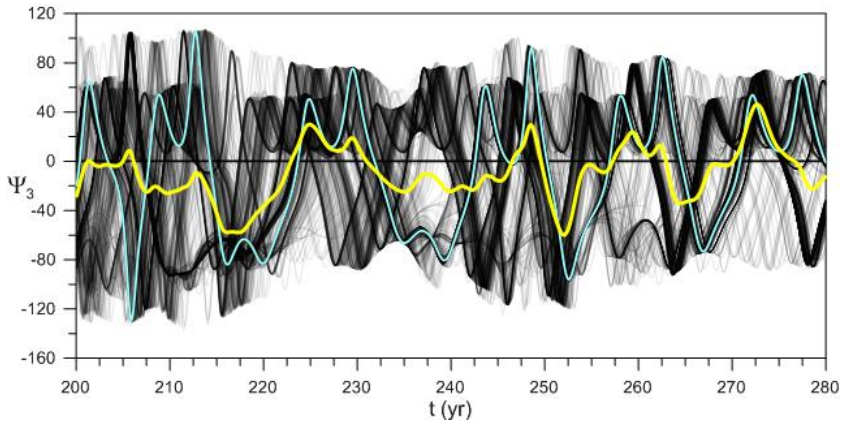

Fig. 5 Black lines: time section of the PBA (ES0) in terms of $\Psi_3(t)$ (only 750 time series, i.e., one out of every 20 among the 15,000 available, is selected for the sake of graphical clarity). The blue line is a single time series belonging to the ensemble represented by black lines; the yellow line gives $\langle\Psi_3\rangle$.

for the specific case under consideration. The black lines show 750 time series $\Psi_3(t)$ among those composing the PBA in the temporal interval $t = 200 - 280\ years$; the yellow line shows $\langle\Psi_3\rangle$ (corresponding to the black line of Fig. 4b), while the blue line is a single time series (belonging to the ensemble represented by black lines) taken as an example. The latter evidences an aperiodic RO modulated by the forcing (Fig. 2c shows the spatial character of this oscillation). The black lines show that the phases of the ROs are not distributed randomly but are, instead, clustered in some groups due to the pacing of the time-dependent forcing. By comparing these clusters with the ensemble mean it can be easily realized that the latter depends strongly on the structure of the intrinsic ROs (for example, compare the yellow line with the black lines within the intervals $t = 210 - 225; 245 - 265\ years$). In conclusion, the ensemble mean depends crucially on intrinsic aspects of the LF variability, therefore it cannot be identified with the FV.

4 Small ensembles of simulations

4.1 Generation of the initial spread (ES1)

As anticipated in section 2.3, the initial data from which ES2-3 is derived are obtained by adopting a classical methodology such as, for example, that used in [32,45-47] to analyse the intrinsic ocean variability with a global eddy-permitting ocean–sea-ice NEMO hindcast. With simulation ES1 (Table 1), a small ES consisting of 50 initial states at $t = 220\ years$ is constructed starting from a point of the PBA at $t = 200\ years$. At that time instant the system can lie in any of the states given by the cyan dots of Fig. 3a, with corresponding $\log_{10} p_i$ shown in Fig. 3b: let us assume that the system actually lies at point P_0 (given by the intersection of a specific trajectory with Ω at $t = 200\ years$) with $\Psi_1 = 26.27, \Psi_2 = 141.54, \Psi_3 = -33.57, \Psi_4 = -7.75$ (Fig. 6). In ES1, 50 forward time integrations starting from P_0 are carried out for 20 years, each member being perturbed by an h (see section 2.1) with a different noise realization, but all with $\varepsilon_3 = 0.2$ and $T_{s3} = 0.5\ years$.

The result is shown by the blue lines of Fig. 6; in Fig. 7a the corresponding Ψ_3–time series are reported. The final points at $t = 220\ years$ (shown in Fig. 7b, in black, superimposed on those of ES0, in cyan) are spread over an area comparable to that of the PBA: these are the initial points of simulations ES2-3.

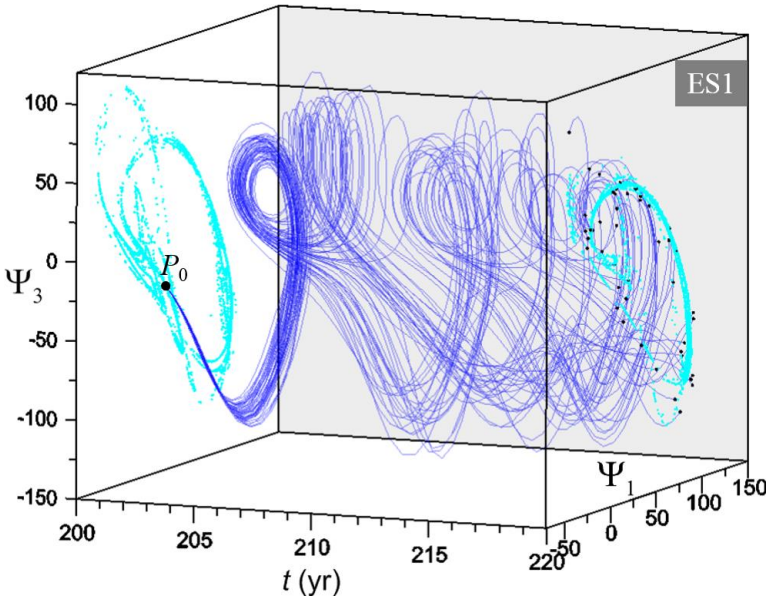

Fig. 6 Evolution of the 50 trajectories of ES1. The black dot at $t = 200\ years$ is the initial point P_0 in Γ. The cyan dots are the intersection of the PBA –as determined by 15,000 trajectories– with Γ at $t = 200, 220\ years$. The black dots at $t = 220\ years$ are the intersection of the 50 trajectories of ES1 with Γ.

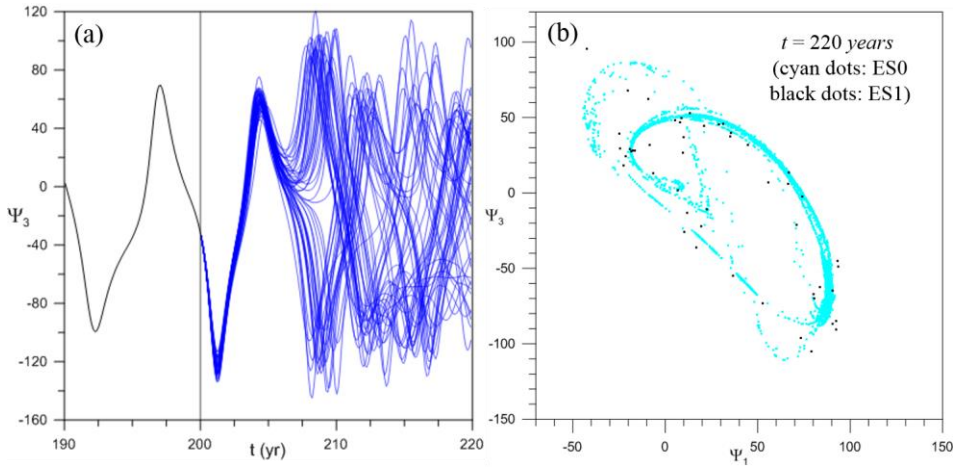

Fig. 7 (a) Ψ_3–time series of ES1 for $t > 200\ years$ (blue lines; the black line corresponds to the trajectory of the PBA lying at P_0 at $t = 200\ years$ chosen for the initialization). (b) Intersection of the PBA (cyan dots) and of the trajectories of ES1 (black dots) with Γ at $t = 220\ years$.

4.2 A deterministic ensemble simulation (ES2)

In ES2 the 50 final points of ES1 at $t = 220\ years$ are integrated for 60 years under the same forcing $\gamma H\mathbf{w}$ of the PBA. The result is shown in terms of the (green) trajectories in Γ in Fig. 8. The MEV and ESV of ES2 are shown in Fig. 9a.

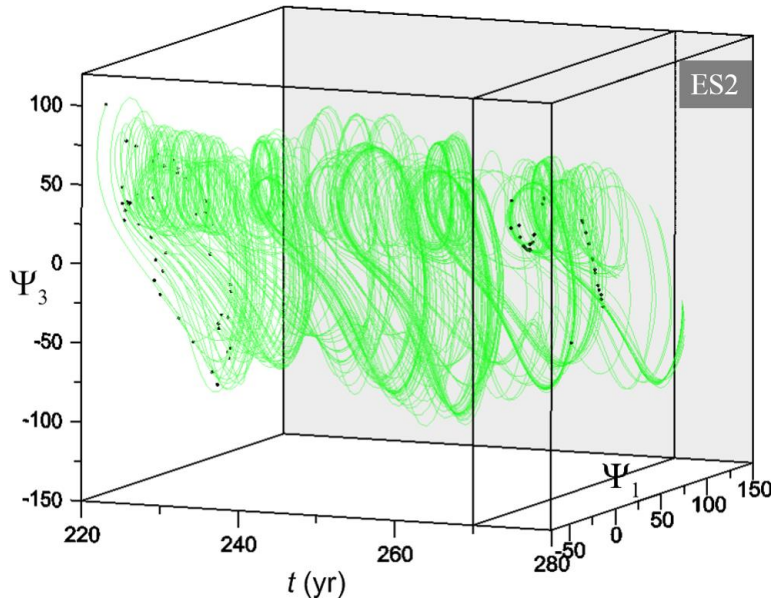

Fig. 8 Evolution of the 50 trajectories of ES2. The black dots are the intersection of the trajectories with Γ at $t = 220\ years$ and $t = 270\ years$.

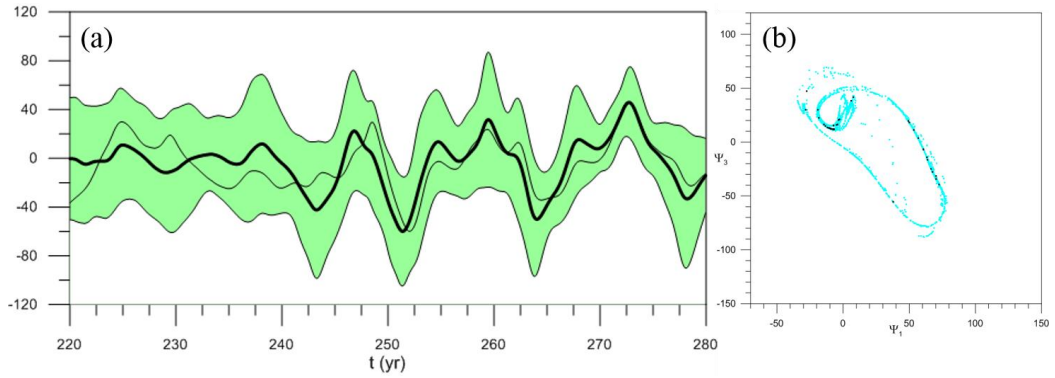

Fig. 9 (a) Thick (thin) line: ensemble mean $\langle\Psi_3\rangle$ of ES2 (ES0). Green shading: interval of twice the ensemble standard deviation σ_{Ψ_3} centred around $\langle\Psi_3\rangle$ for ES2. (b) Intersection of the PBA (cyan dots) and of the trajectories of ES2 (black dots) with Γ at $t = 270\ years$.

Comparison of $\langle\Psi_3\rangle$ (thick line) with the corresponding quantity for ES0 (thin line) shows that the MEV of ES2 provides a good approximation of the same quantity derived from the PBA already after $\approx 20\ years$ of integration (basically the predictability time characterizing the PBA, see section 3) despite the much smaller number of members. The difference is mainly in the MEV, which is now

smaller ($\sigma_{MEV} = 22.77$; $\sigma_{ESV} = 38.15$, the ratio Z is in fact slightly smaller: $Z^{(ES2)} = 0.60$ vs $Z^{(ES0)} = 0.73$), but it should be reminded that $Z^{(ES0)}$ is computed over the whole 400 years of the PBA. Fig. 9b shows that the initial departure from the PBA (Fig. 7b) is soon removed during ES2.

4.3 A random ensemble simulation (ES3)

As already seen, the main problem arising in the determination of the FV and IV from the ensemble mean and spread is the pacing effects induced by the full forcing, which lead to the clustering of RO phases, as evident in Fig. 5 for ES0 and in Fig. 9a for ES2. With reference to ES2, it could be conjectured that if the forcing were perturbed by a noise -each ensemble member being subjected to a different realization- the pacing would occur differently in each of them. If, in addition, such perturbations were sufficiently weak not to modify substantially the character of the variability, then the ESV could possibly provide a better estimate of the IV. With the random simulation ES3 this conjecture is explored; a future quantitative study relying also on synchronization quantifiers [e.g., 48] will be needed to explore the applicability and effectiveness of the proposed methodology.

ES3, differs from ES2 only in that, now, $G/\gamma = H + h$, where h is a red noise with $\varepsilon_3 = 0.1, T_{s3} = 1\ year$ and, like in ES1, a different realization of the stochastic process is adopted for each member. The result is shown in terms of the (magenta) trajectories in Γ in Fig. 10. It is immediately evident that the RO phases are indeed more randomly distributed than in ES0 and ES2. In addition, the trajectories do not converge toward the PBA as effectively as in ES2 because of the different forcing, but they do remain close to the latter thanks to the small amplitude of the perturbation, as shown in Fig. 11b at $t = 270\ years$ (see section 6 for a detailed analysis of this aspect).

The MEV and ESV are reported in Fig. 11a. Unlike for ES2, the MEV (thick line) is substantially different from that of the PBA (thin line). As for the rms variabilities for ES2/3 one has $\sigma_{MEV}^{(ES2)} = 22.8$, $\sigma_{MEV}^{(ES3)} = 13.6$ and $\sigma_{ESV}^{(ES2)} = 38.1$, $\sigma_{ESV}^{(ES3)} = 42.6$, so that $Z^{(ES2)} = 0.6$, $Z^{(ES3)} = 0.32$. The ESV is, therefore, comparable in the two cases: this confirms that the character of the variability is

similar (apart from the phases) in ES2 and ES3. On the contrary, the MEV in ES3 is reduced by ~60% in comparison with that of ES2.

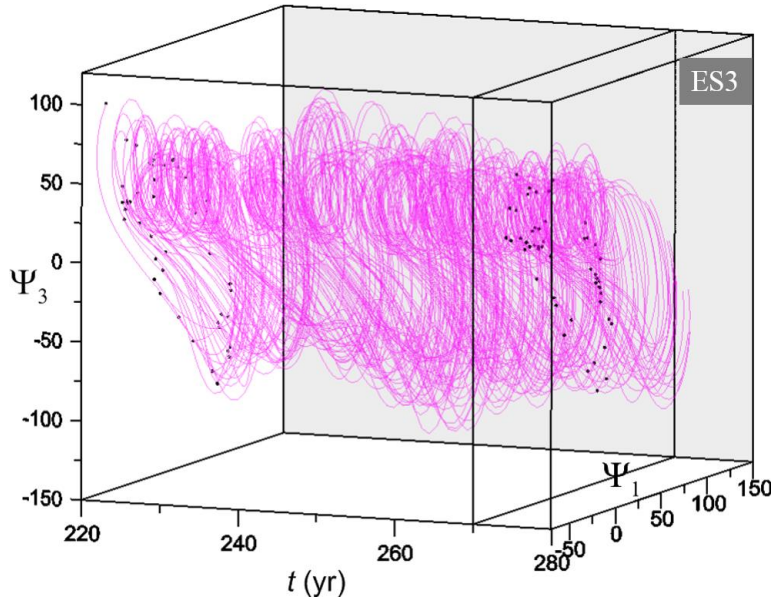

Fig. 10 Evolution of the 50 trajectories of ES3. The black dots are the intersection of the trajectories with Γ at $t = 220\ years$ and $t = 270\ years$.

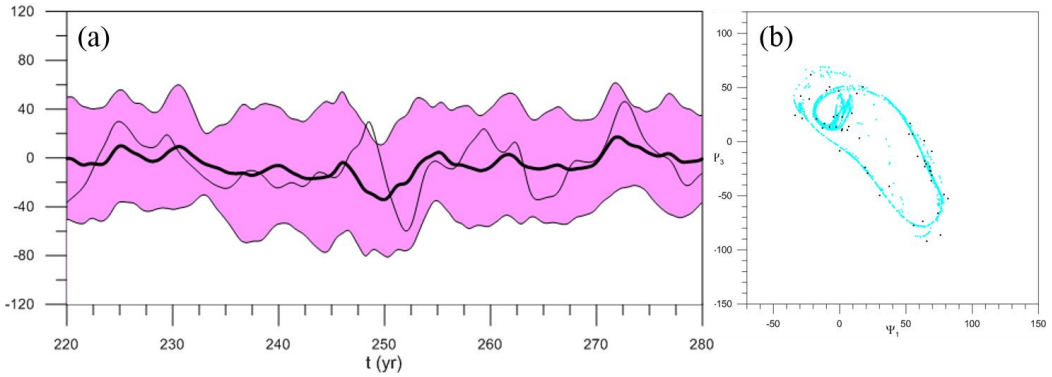

Fig. 11 (a) Thick (thin) line: ensemble mean $\langle\Psi_3\rangle$ of ES3 (ES0). Green shading: interval of twice the ensemble standard deviation σ_{Ψ_3} centred around $\langle\Psi_3\rangle$ for ES3. (b) Intersection of the PBA (cyan dots) and of the trajectories of ES3 (black dots) with Γ at $t = 270\ years$.

Thus, the FV, deprived however of the important pacing effect of the intrinsic ROs, is likely to be better represented by $\langle\Psi_3\rangle^{(ES3)}$ than by $\langle\Psi_3\rangle^{(ES2)}$; at the same time, the ESV is close to that of ES2 and therefore of ES0. This suggests that $\langle\Psi_3\rangle^{(ES3)}$ might in fact be used to extract a better statistical representation of the IV compared to that obtainable from ES2. However, in a nonlinear context, the phasing of the ROs (a very important aspect of the FV greatly reduced by the procedure) cannot be

singled out from the overall effect of the total forcing $H + h$, and this, in turn, affects the IV as well: this is a subtle aspect that should be investigated in a future study.

5 Sensitivity to initial data (ES4-6)

Still in the framework of issue (ii), in simulations ES4-6 the sensitivity of the MEV and ESV to the distribution of initial data is investigated. Assessing to what degree the initial data are representative of all the states the system can assume at a specific time instant is clearly an important issue. If, for example, the initial data were clustered in a limited region of the PBA, the system might not explore extended regions of the latter during the subsequent forward time integration, which is necessarily of limited temporal extent (in a sufficiently long integration the attractor would be, eventually, densely covered thanks to the system's chaoticity, except if the initialization is limited to regions of Γ in which the normalized distance as defined in [14,27], is smaller than unity, which is never the case of the present initializations).

To analyse this aspect, in ES4 (Table 1) ES1 is replicated by choosing a smaller stochastic perturbation h (now $\varepsilon_3 = 0.05$ instead of $\varepsilon_3 = 0.2$). This produces a smaller spread, as evident by comparing Fig. 12 with Fig. 6 and Fig. 13 with Fig. 7. The ROs are now basically clustered in two groups (Fig. 13a) unlike the more random distribution of the RO phases in ES1 (Fig. 7a). Moreover, comparison of Fig. 13b with Fig. 7b shows that the spread of the final (black) points is reduced in ES4 compared with ES1 (in the latter case the black dots are spread over an area comparable to that of the PBA) but, at the same time, in ES1 the points depart from the attractor more than in ES4 and this will in turn require a longer time for convergence to the PBA. This suggests that choosing large amplitudes of h implies two competing effects and should, therefore, be considered with caution.

The subsequent evolution is given by ES5-6, which correspond to ES2-3, respectively, except for the initial data, now provided by ES4 instead of ES1. The results are summarized in Fig.

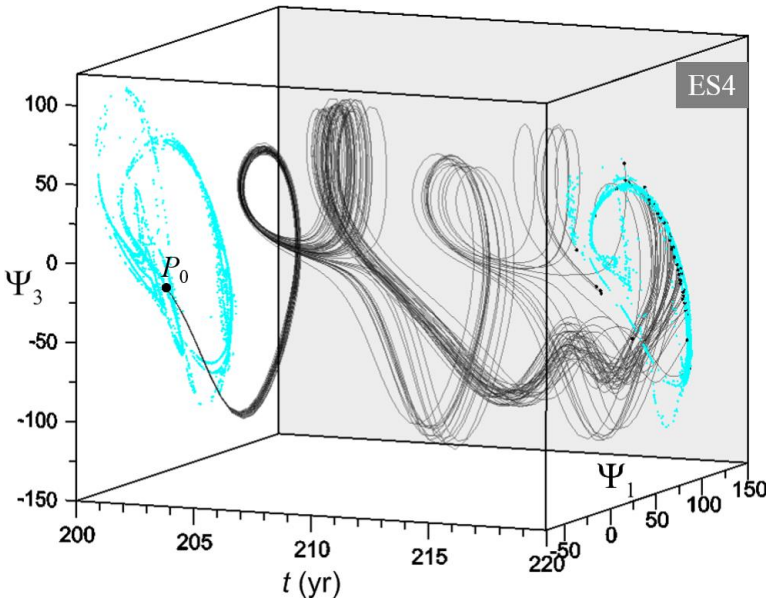

Fig. 12 Evolution of the 50 trajectories of ES4. The black dot at $t = 200\ years$ is the initial point P_0 in Γ. The cyan dots are the intersection of the PBA –as determined by 15,000 trajectories– with Γ at $t = 200, 220\ years$. The black dots at $t = 220\ years$ are the intersection of the 50 trajectories of ES4 with Γ.

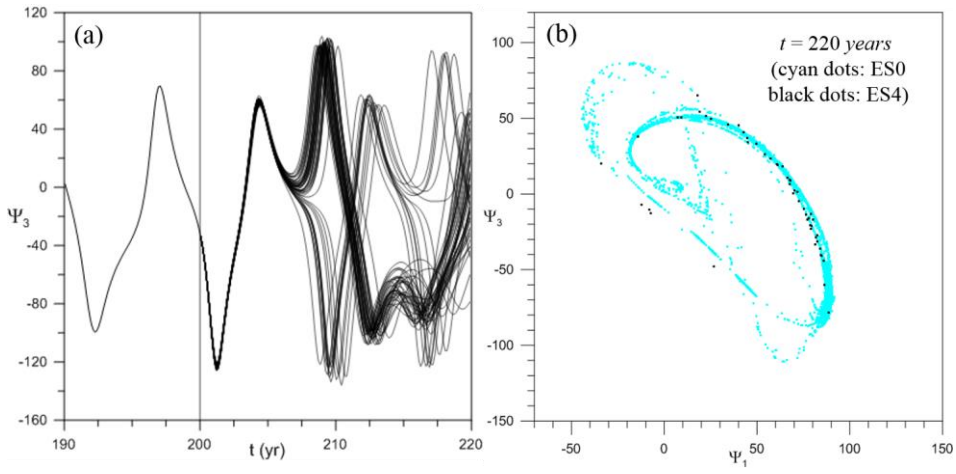

Fig. 13 (a) Ψ_3–time series of ES4 for $t > 200\ years$ (the line for $t < 200\ years$ corresponds to the trajectory of the PBA lying at P_0 at $t = 200\ years$ chosen for the initialization). (b) Intersection of the PBA (cyan dots) and of the trajectories of ES4 (black dots) with Γ at $t = 220\ years$.

14: the impact of the limited initial spread is felt strongly in the deterministic simulation ES5 for $t \lesssim 245\ years$ but it is much smaller for larger times (compare Fig. 14a with Fig. 9a). A similar conclusion can be drawn from the random simulation ES6 (compare Fig. 14b with Fig. 11a). Thus, simulations ES4-6 show that a reduced initial spread can greatly affect the ensemble mean and spread for the first few decades of integration, but this effect is reduced during the following evolution, when the chaotic character of the system has had enough time to act.

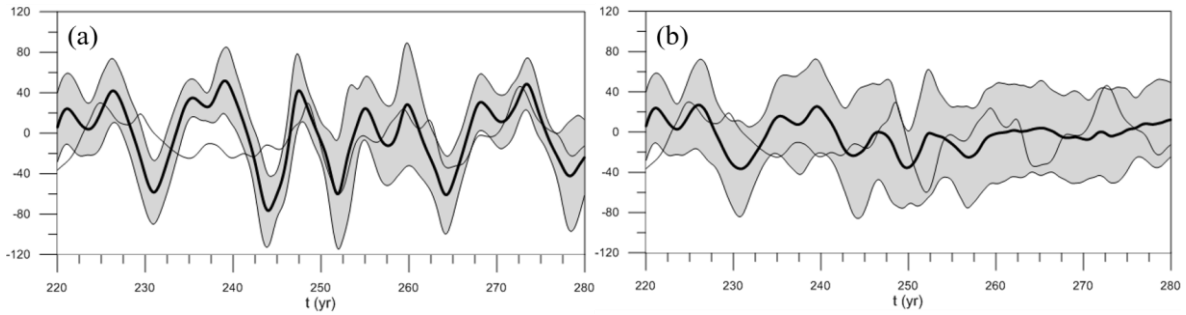

Fig. 14 (a) Thick (thin) line: ensemble mean $\langle \Psi_3 \rangle$ of ES5 (ES0). Grey shading: interval of twice the ensemble standard deviation σ_{Ψ_3} centred around $\langle \Psi_3 \rangle$ for ES5. (b) as in (a) but for ES6.

6 Analysis of the convergence to the pullback attractor

Still in the framework of issue (ii), the process of (typically exponential) convergence of the small ESs to the PBA is investigated in this section. This aspect is of fundamental importance in climate change studies [e.g., 11] and has been occasionally considered in the preceding sections. Here, a more systematic and general analysis based also on some novel time-dependent quantifiers is presented and discussed.

A first classical statistical tool is the system's entropy as defined in information theory [49],

$$S_{ES}(t) = -\sum_i p_i \ln p_i. \tag{7}$$

S_{ES} (henceforth the ES is indicated as a subscript) measures the degree of system's order and, therefore, provides a valuable indication about the statistical distribution of the ensemble members in phase space. The probability $p_i(t)$ in (7) is defined in section 3 (the sum is clearly extended to the cells with $p_i \neq 0$), but here the grid has a larger step ($\Delta\Psi_1 = \Delta\Psi_3 = 5$) to account for the small number of ensemble members in ES1-6. In Fig. 15a, the entropy S_{ES0} of the PBA is shown by the black line; S_{ES1} (blue line) starts from 0 at $t = 200\ years$, when all the trajectories lie in a single cell containing P_0 and reaches values comparable to S_{ES0} already at $t{\sim}210\ years$. S_{ES2} (green line) follows the temporal dependence of S_{ES0} from $t \gtrsim 255\ years$, suggesting that convergence to the PBA has occurred, but it is systematically smaller than S_{ES0} because the number of ensemble

members in ES2 is much smaller than that of ES0, so that the PBA cannot be densely covered by ES2; yet, full convergence onto the PBA of the 50 trajectories is nonetheless achieved, as shown, for example, in Fig. 9b for $t = 270\ years$. As for ES3 (magenta line), the stochastic perturbation prevents full convergence, as it increases the spread (so that S_{ES3} is larger than S_{ES0}) and reduces the entropy variability, since the RO clustering (the origin of the LFV in S_{ES0} and S_{ES2}) is also reduced.

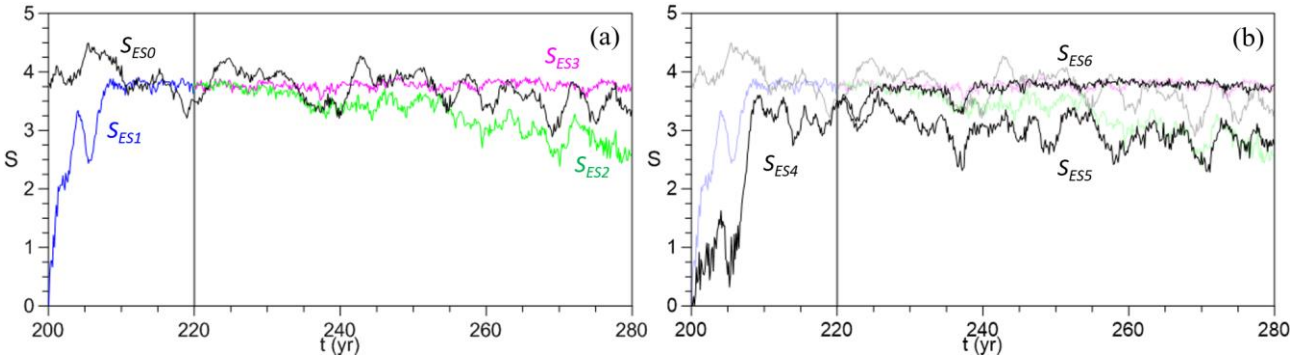

Fig. 15 Time series of the entropy as defined in (7) for ES0-3 (a) and ES4-6 (b). The lines of panel (a) are included in panel (b) with fainter colours for the sake of comparison.

Fig. 15b shows the same quantities for ES4-6. The reduced initial spread at $t = 220\ years$ (compare S_{ES4} with S_{ES1}) leads to a reduced S_{ES5} compared to S_{ES2} for the first three decades, but the two entropies virtually coincide afterwards; again, the chaotic system's behaviour makes the asymptotic evolution statistically independent of the initialization. On the other hand, S_{ES6} tends to coincide with S_{ES3} just few years after $t = 220\ years$ due to the stochastic perturbation in the external forcing. The entropies are thus consistent with the conclusions drawn in sections 4-5 and complement them with time-dependent statistical information about the ES spread.

The ES entropy is a valuable statistical tool but it does not provide any direct information about the convergence of the ES to the PBA (two probability distributions could have the same entropy and be completely disjoint). Additional information to this respect can be given by the parameters R and D, which are now introduced. The first is:

$$R_{ES}(t) = \frac{m_{ES}}{n_{ES}}, \tag{8}$$

where

$$m_{ES} = \sum_i a_i \,;\;\; a_i = \begin{cases} 1 \;\; if \;\; q_i \neq 0 \; and \; p_i \neq 0 \\ 0 \;\; otherwise \end{cases} \;\; ; \;\; n_{ES} = \sum_i b_i \,;\;\; b_i = \begin{cases} 1 \;\; if \; p_i \neq 0 \\ 0 \;\; otherwise \end{cases} \qquad (9)$$

in which q_i and p_i are the probabilities of localization of the trajectories of ES0 and ES in Γ, respectively. Thus m_{ES} is the number of cells that are occupied by at least one member of *both* ES and ES0 while n_{ES} is the number of cells occupied by at least one member of ES, so that $R_{ES} = 1$ if all the trajectories have converged to the PBA while $R_{ES} = 0$ if they all lie outside the PBA (here, as for S_{ES}, $\Delta\Psi_1 = \Delta\Psi_3 = 5$ is found to be an optimal choice in consideration of the differing number of members of ES0 and of ES1-6).

Fig. 16a shows R for ES1-3. $R_{ES1} = 1$ initially because all the 50 initial points lie in P_0; the random perturbation h prevents convergence to the PBA, so that, at $t = 220\ years$ only ~60% of the points lie on the latter (Fig. 7b). The further evolution under a similar random forcing (ES3, magenta line) does not modify substantially the situation. Instead, the evolution subjected to the same forcing of the PBA (ES2) leads the trajectories to rapidly converge to the latter, as shown by the green line ($R_{ES2} \cong 1$ after $t \gtrsim 230\ years$). Fig. 16b shows R for ES4-6: the reduced initial spread at $t = 220\ years$ (Fig. 15b) leads to a nearly instantaneous convergence of ES5 to the PBA, while the randomly forced evolution (ES6) does not differ substantially from that of ES3.

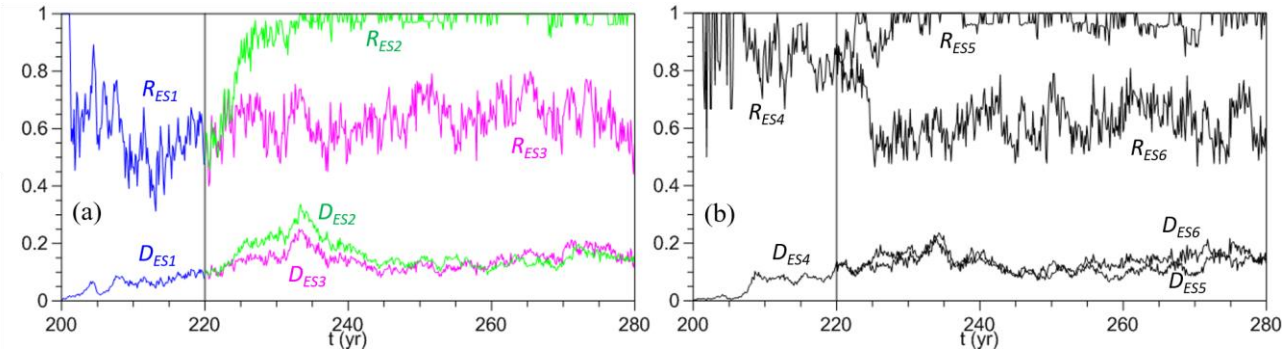

Fig. 16 Time series of the parameters R and D as defined in (8) and (10), respectively, for ES1-3 (a) and ES4-6 (b).

Another useful parameter is:

$$D_{ES}(t) = \frac{m_{ES}}{n_{ES0}} \;\; ; \;\; n_{ES0} = \sum_i c_i \,;\;\; c_i = \begin{cases} 1 \;\; if \; q_i \neq 0 \\ 0 \;\; otherwise \end{cases}. \qquad (10)$$

D informs about the degree of coverage of the PBA; for example, virtually all the ES2-ensemble members converge to the PBA ($R_{ES2} \cong 1$, Fig. 16a) but D shows that only ~15% of the cells occupied by the latter are also occupied by ES2 ($D_{ES2} \cong 0.15$, Fig. 16a).

It is interesting to note that the random ES3 and ES6 attain a degree of coverage of the PBA comparable to that of the corresponding deterministic ES2 and ES5 (Fig. 16), despite the substantially different values of R. To understand how this is possible let us consider, for example, ES2 and ES3 at $t = 270\ years$ (see Figs. 9b and 11b): $n_{ES2} = 24$, $n_{ES3} = 45$, $m_{ES2} = 24$, $m_{ES3} = 29$ and $n_{ES0} = 173$. In ES3 many more cells are occupied than in ES2 (45 vs. 24) while a comparable number of cells belonging to ES0 are occupied in the two cases (29 vs. 24), so $D_{ES2} \cong D_{ES3}$; however, for ES3 each cell shared with ES0 is occupied by just ~1 point on average, compared with ~2 points for ES2.

This example suggests that a complementary information about the convergence should consider the number of points falling in each grid cell: this implies the evaluation of an appropriate distance between the probability distributions **q** and **p**. The so-called Wasserstein distance is now being used in some studies of climate dynamics [e.g., 8,50]; however, its application to the present case is problematic because of the extremely large difference between the two data samplings. An alternative procedure is thus adopted.

The following parameter is first introduced:

$$Q_{ES}(t) = 1 - \frac{1}{2}\sum_i |q_i - p_i|. \tag{11}$$

In Q the metric $\sum_i |q_i - p_i|$ measures the distance between **q** and **p**. If they coincide (perfect statistical convergence), $Q_{ES} = 1$; if, on the contrary, they are totally disjoint ($q_i = 0$ if $p_i \neq 0$ and vice versa), $Q_{ES} = 0$. However, in consideration of the very small number of ensemble members contributing to **p**, significant statistical convergence can never be achieved; therefore, a more useful parameter appears to be:

$$\tilde{Q}_{ES}(t) = 1 - \frac{1}{2}\sum_i |\tilde{q}_i - p_i|; \quad \tilde{q}_i = \frac{q_i a_i}{\sum_k q_k a_k}, \tag{12}$$

[with a_i defined in (9)], where $\tilde{q}_i$ refers only to the cells that are occupied by both ES and ES0. Thus, $\tilde{Q}_{ES}$ measures the statistical convergence of ES to ES0 in the m_{ES} common cells.

In Fig. 17, $\tilde{Q}$ is reported for ES1-6. In Fig. 17a, ES1 yields perfect coincidence at $t = 200\ years$ (all trajectories lie on P_0), with $\tilde{Q}_{ES1}$ decreasing due to the random forcing until the degree of similarity stabilises about 10 $years$ before the end of the ES. The subsequent evolution in the random ES3 leaves $\tilde{Q}$ basically unaltered on average; on the contrary, ES2 yields, as obvious, an increasing degree of statistical convergence. It is worth noting that, although virtually all trajectories lie on the PBA for $t \gtrsim 230\ years$ (see R_{ES2} in Fig. 16a), $\tilde{Q}_{ES2}$ is appreciably less than unity: this is because **p** is too undersampled compared with **q**; in fact one would have $\tilde{Q}_{ES2} \to 1$ as $N_{ES} \to N$. Finally, Fig. 17b shows that $\tilde{Q}_{ES4}$ and $\tilde{Q}_{ES6}$ do not differ substantially from $\tilde{Q}_{ES1}$ and $\tilde{Q}_{ES3}$, respectively, apart near the matching time $t = 220\ years$. On the other hand, $\tilde{Q}_{ES5}$ is appreciably smaller than $\tilde{Q}_{ES2}$ for $t \gtrsim 260\ years$: this is because the trajectories tend, more in ES2 than in ES5, to clusterize in regions of the PBA where $\tilde{q}_i$ is higher (to understand this, one can note that, e.g., in the interval $t = 265 - 280\ years$, the width of the line bundle for ES0 -Fig. 5- is closer to that of ES2 than that of ES5). This implies, locally, a better sampling of p_i which, in turn, leads to $\tilde{Q}_{ES5} < \tilde{Q}_{ES2}$.

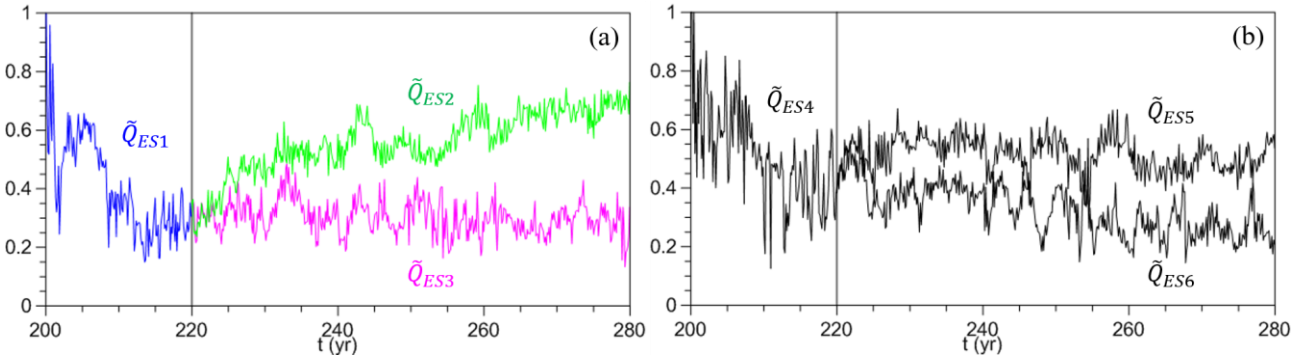

Fig. 17 Time series of the parameter $\tilde{Q}$ as defined in (12) for ES1-3 (a) and ES4-6 (b).

In conclusion, the system's entropy $S(t)$ and the additional parameters $R(t)$, $D(t)$ and $\tilde{Q}(t)$ have allowed to monitor the convergence of ES1-6 to the PBA. Due to the great difference in the data sampling between the small ESs and the PBA, the convergence process cannot be adequately described by a single quantifier; the combined use of these four parameters has instead proved to be suitable for a complete description of the process.

7 Conclusions

In this paper, the PBA of an excitable conceptual ocean model subjected to an aperiodic external forcing, whose variability has both low- (decadal time-scale) as well as higher frequency fluctuations, has been determined through a large ES; this is nowadays acknowledged to be the correct mathematical approach to analyse climate changes.

The PBA is first used to analyse a crucial aspect of climate dynamics [issue (i)]: the identification of the system's IV, i.e., of that part of the variability that is not due to a passive response to variations of the external forcing but rather to nonlinear mechanisms all internal to the climate system. To this respect, it is important to note that the case considered here differs from the classical long-term climate projections obtained with ESs based on intermediate-complexity (single) climate models.

In those studies, the varying external forcing is typically the CO_2 concentration, which does not present any fluctuation and is assumed to double over a long time period (e.g., $100\ years$) in order to represent the main anthropogenic forcing, as done, for example in [10,13,15]. In such a case the ensemble mean of a generic climate parameter yields the same regularity of the temporal dependence of the forcing, while the ensemble spread, measured by the instantaneous ensemble standard deviation, is a highly variable signal with multiple time scales (see, for example, [13] and Fig. 1 therein). Such a clear scale separation between the ensemble mean and spread makes them unambiguously representative of the system's FV and IV, respectively.

In contrast, the present case study is a hindcast in which the forcing includes a full range of time scales (Fig. 1); in parallel, the resulting ensemble mean and spread yield complex temporal structures without any clear scale separation, as shown in Fig. 4 (this condition is similar, e.g., to the NEMO-hindcast ES [46,32,45,47]). Now, the system's intrinsic ROs can be paced, and therefore clustered over the PBA under the effect of the time dependent forcing [26,37,14], as discussed in section 3. Thus, the ensemble mean cannot be simply identified with the FV because it depends substantially on internal dynamical mechanisms; in turn, the FV and IV cannot in this case be unambiguously separated. This result suggests that caution should be taken in identifying the FV and IV with the ensemble mean and spread in climate phenomena in which the time-dependent external forcing interacts substantially with internal modes of variability. Of course, the ensemble mean and spread are always valuable parameters irrespective of their relation with the FV and IV.

The other aspect dealt with in this paper concerns the relevance of the number of ensemble members N on the statistical significance of the ESs [issue (ii)]. Since intermediate-complexity climate models currently impose $N = O(10^2)$, a natural question arises: to what degree are such ESs approximating the respective PBA? Obviously, this question remains without answer in the original context, but what can be done is to use a conceptual case study, in which the PBA can be accurately determined, and then construct small ESs to analyse their departure from, and convergence to, the PBA. A study of this kind has been done here for the first time (at the best of the author's knowledge) with a conceptual model. To analyse the process of convergence, three parameters have been specifically designed: $R(t)$, which gives the relative number of ensemble members that have converged to the PBA, $D(t)$, which measures the degree of coverage of the PBA by the ensemble members and $\tilde{Q}(t)$, which provides a statistical measure of the similarity. The results reveal a remarkable significance of the small ESs after a time from their initializations that is basically coincident with the system's predictability time.

Future extensions include an assessment of the system's predictability as a function of the location of the initial state on the PBA, an analysis of how this can be performed with small ESs, studies in which the external forcing and parameter values are modified.

Acknowledgments

This work was funded by the MOMA (PNRA16_00196) and IPSODES (PNRA18_00199-C) projects of the Italian "Programma Nazionale di Ricerche in Antartide". Support from the University of Naples Parthenope (contract n. DSTE315B) is also kindly acknowledged.

References

1. Ghil, M., Chekroun, M. D., Simonnet, E.: Climate dynamics and fluid mechanics: Natural variability and related uncertainties. Physica D 237, 2111–2126 (2008)

2. Pierrehumbert, R.T.: Principles of Planetary Climate. Cambridge University Press, 674 pp (2010)

3. Chekroun, M.D., Simonnet, E., Ghil, M.: Stochastic climate dynamics: Random attractors and time-dependent invariant measures. Physica D 240, 1685–1700 (2011)

4. Bódai, T., Károlyi, G., Tél, T.: A chaotically driven model climate: Extreme events and snapshot attractors. Nonlin. Processes Geophys. 18, 573–580 (2011)

5. Bódai, T., Károlyi, G., Tél, T.: Fractal snapshot components in chaos induced by strong noise. Phys. Rev. 83E, 046201 (2011)

6. Bódai, T., Tél, T.: Annual variability in a conceptual climate model: Snapshot attractors, hysteresis in extreme events, and climate sensitivity. Chaos 22, 023110 (2012)

7. Ghil, M.: The complex physics of climate change and climate sensitivity: A grand unification (Alfred Wegener Medal Lecture). European Geosciences Union General Assembly 2012, Vienna, Austria, European Geosciences Union, EGU2012-14438-1 (2012)

8. Ghil, M.: A Mathematical Theory of Climate Sensitivity or, How to Deal With Both Anthropogenic Forcing and Natural Variability? In: Climate Change: Multidecadal and Beyond, edited by: Chang, C.-P., Ghil, M., Latif, M., and Wallace, J., World Scientific Publishing Co., Singapore, 6, 31–52 (2015)

9. Daron, J.D., Stainforth, D.A.: On quantifying the climate of the nonautonomous Lorenz-63 model. Chaos 25, 043103 (2015)

10. Drótos, G., Bódai, T., Tél, T.: Probabilistic concepts in a changing climate: A snapshot attractor picture. J. Climate 28, 3275–3288 (2015)

11. Drótos, G., Bódai, T., Tél, T.: On the importance of the convergence to climate attractors. Eur. Phys. J. Spec. Top. 226, 2031-2038 (2017)

12. Ragone, F., Lucarini, V., Lunkeit, F.: A new framework for climate sensitivity and prediction: A modelling perspective. Climate Dyn. 46, 1459-1471 (2016)

13. Herein, M., Márfy, J., Drótos, G., Tél, T.: Probabilistic Concepts in Intermediate-Complexity Climate Models: A Snapshot Attractor Picture. J. Climate 29, 259-272 (2016)

14. Pierini, S., Ghil, M., Chekroun, M.D.: Exploring the pullback attractors of a low-order quasigeostrophic ocean model: the deterministic case. J. Climate 29, 4185-4202 (2016)

15. Herein, M., Drótos, G., Haszpra, T., Márfy, J., Tél, T.: The theory of parallel climate realizations as a new framework for teleconnection analysis. Sci. Rep. 7, 44529 (2017)

16. Ghil, M.: A century of nonlinearity in the geosciences. Earth Space Sci. 6, 1007–1042 (2019)

17. Stocker, T.F., et al., Eds.: Climate Change 2013 (IPCC): The Physical Science Basis. Cambridge University Press, 1535 pp (2013)

18. Drótos, G., Bódai, T., Tél, T.: Quantifying nonergodicity in nonautonomous dissipative dynamical systems: An application to climate change, Phys. Rev. E 94, 022214 (2016)

19. Eckmann, J.-P., Ruelle, D.: Ergodic theory of chaos and strange attractors. Rev. Mod. Phys., 57, 617–656 (1985)

20. Nicolis, G.: Introduction to Nonlinear Science. Cambridge University Press, Cambridge, UK (1995)

21. Ott, E.: Chaos in Dynamical Systems. Cambridge University Press, 478 pp (2002)

22. Tél, T., Gruiz, M.: Chaotic Dynamics. Cambridge University Press, Cambridge, UK (2006)

23. Strogatz, S. H.: Nonlinear Dynamics and Chaos: with Applications to Physics, Biology, Chemistry, and Engineering. CRC Press, Boca Raton, FL, USA (2015)

24. Dijkstra, H.A., Ghil, M.: Low-frequency variability of the large-scale ocean circulation: A dynamical systems approach. Rev. Geophys. 43, RG3002 (2005)

25. Ghil, M.: The wind-driven ocean circulation: Applying dynamical systems theory to a climate problem. Discr. Cont. Dyn. Syst. A 37, 189–228 (2017)

26. Pierini, S.: Low-frequency variability, coherence resonance and phase selection in a low-order model of the wind-driven ocean circulation. J. Phys. Oceanogr. 41, 1585–1604 (2011)

27. Pierini, S., Chekroun, M.D., Ghil, M.: The onset of chaos in nonautonomous dissipative dynamical systems: A low-order ocean–model case study. Nonlin. Processes Geophys. 25, 671-692 (2018)

28. Pikovsky, A.S., Kurths, J.: Coherence resonance in noise-driven excitable systems. Phys. Rev. Lett. 78, 775–778 (1997)

29. Pierini, S.: Coherence resonance in a double-gyre model of the Kuroshio Extension. J. Phys. Oceanogr. 40, 238–248 (2010)

30. Crucifix, M.: Oscillators and relaxation phenomena in Pleistocene climate theory. Phil. Trans. R. Soc. A370, 1140-1165 (2012)

31. Van der Pol, B.: On relaxation-oscillations. The London, Edinburgh and Dublin Phil. Mag. J. Sci. 2, 978–992 (1926)

32. Bessières, L., Leroux, S., Brankart, J.-M., Molines, J.-M., Moine, M.-P., Bouttier, P.-A., Penduff, T., Terray, L., Barnier, B., Sérazin, G.: Development of a probabilistic ocean modelling system based on NEMO 3.5: application at eddying resolution. Geosci. Model Dev. 10, 1091–1106 (2017)

33. Maher, N., Milinski, S., Suarez-Gutierrez, L., Botzet, M., Dobrynin, M., Kornblueh, L., Kröger, J., Takano, Y., Ghosh, R., Hedemann, C., Li, C., Li, H., Manzini, E., Notz, D., Putrasahan, D., Boysen, L., Claussen, M., Ilyina, T., Olonscheck, D., Raddatz, T., Stevens, B., Marotzke, J.: The Max Planck Institute Grand Ensemble: Enabling the Exploration of Climate System Variability, J. Adv. Mod. Earth Sys. 11, https://doi.org/10.1029/2019MS001639 (2019)

34. Pierini, S.: A Kuroshio Extension System model study: decadal chaotic self-sustained oscillations. J. Phys. Oceanogr. 36, 1605-1625 (2006)

35. Pierini, S.: On the crucial role of basin geometry in double-gyre models of the Kuroshio Extension. J. Phys. Oceanogr. 38, 1327–1333 (2008)

36. Pierini, S., Dijkstra, H.A.: Low-frequency variability of the Kuroshio Extension. Nonlin. Processes Geophys. 16, 665–675 (2009)

37. Pierini, S.: Stochastic tipping points in climate dynamics. Phys. Rev. E 85, 027101 (2012)

38. Pierini, S.: Ensemble simulations and pullback attractors of a periodically forced double-gyre system. J. Phys. Oceanogr. 44, 3245-3254 (2014)

39. Vannitsem, S., De Cruz, L.: A 24-variable low-order coupled ocean–atmosphere model: OA-QG-WS v2. Geosci. Model Dev. 7, 649–662 (2014)

40. De Cruz, L., Schubert, S., Demaeyer, J., Lucarini, V., Vannitsem, S.: Exploring the Lyapunov instability properties of high-dimensional atmospheric and climate models, Nonlin. Processes Geophys. 25, 387–412 (2018)

41. Vallis, G. K.: Atmospheric and Oceanic Fluid Dynamics. Cambridge University Press, 745 pp (2006)

42. Arnold, L.: Random Dynamical Systems. Springer, 586 pp (1998)

43. Rasmussen, M.: Attractivity and Bifurcation for Nonautonomous Dynamical Systems. Springer, 217 pp (2007)

44. Bódai, T., Károlyi, G., Tél, T.: Driving a conceptual model climate by different processes: Snapshot attractors and extreme events. Phys. Rev. E 87, 022822 (2013)

45. Sérazin, G., Jaymond, A., Leroux, S., Penduff, T., Bessières, L., Llovel, W., Barnier, B., Molines, J.-M., Terray, L.: A global probabilistic study of the ocean heat content low-frequency variability: Atmospheric forcing versus oceanic chaos. Geophys. Res. Lett. 44, 5580–5589 (2017)

46. Penduff, T., Barnier, B., Terray, L., Sérazin, G., Gregorio, S., Brankart, J.-M., Moine, M.-P., Molines, J.-M., Brasseur, P.: Ensembles of eddying ocean simulations for climate. CLIVAR Exchanges No.65, Vol. 19, No. 2 (2014)

47. Leroux, S., Penduff, T., Bessières, L., Molines, J.-M., Brankart, J.-M., Sérazin, G., Barnier, B., Terray, L.: Intrinsic and Atmospherically Forced Variability of the AMOC: Insights from a Large-Ensemble Ocean Hindcast. J. Climate 31, 1183-1203 (2018)

48. Pikovsky, A., Rosenblum, M., Kurths, J.: Synchronization: A universal concept in nonlinear sciences. Cambridge Nonlinear Science Series 12, Cambridge University Press, Cambridge, UK (2003)

49. Shannon, C. E.: The mathematical theory of communication. Bell Syst. Tech. J. 27, 379–423 (1948)

50. Vissio, G., Lucarini, V.: Evaluating a stochastic parametrization for a fast–slow system using the Wasserstein distance. Nonlin. Processes Geophys. 25, 413–427 (2018)